

Highly Dispersed Ni⁰/Ni_xMg_{1-x}O Catalysts Derived from Solid Solutions: How Metal and Support Control the CO₂ Hydrogenation

Marie-Mathilde Millet,[†] Andrey V. Tarasov,[†] Frank Girgsdies,[†] Gerardo Algara-Siller,[†] Robert Schlögl,^{†,‡} and Elias Frei^{*,†}

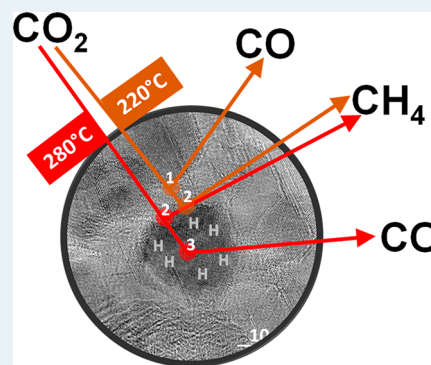
[†]Department of Inorganic Chemistry, Fritz-Haber-Institut der Max-Planck-Gesellschaft, Faradayweg 4-6, 14195 Berlin, Germany

[‡]Max-Planck-Institut für Chemische Energiekonversion, Abteilung Heterogene Reaktionen, Stiftstr. 34-36, 45470 Mülheim an der Ruhr, Germany

Supporting Information

ABSTRACT: Among the Ni-based catalysts studied for CO₂ activation reactions, Ni_xMg_{1-x}O solid solutions present advantageous characteristics, mainly linked with the homogeneous distribution of the Ni species inside the MgO structure, leading to highly dispersed Ni⁰ supported catalysts. In this work, we report on the preparation and characterization of Ni_xMg_{1-x}O precatalysts calcined at different temperatures. The resulting Ni⁰/Ni_xMg_{1-x}O catalysts were tested for the methanation of CO₂. Following the structural, morphological, and chemical changes during both the calcination and the reduction, we were able to observe clear correlations between the reactivity of the catalysts and their physical properties, leading to a better understanding of the reaction mechanism and the respective contributions of the metal and the support. While no change was observed in the formation of CH₄ over the range of temperature tested, the CO formation as byproduct clearly changed with the increasing temperatures. Our results are consistent with the hypothesis that two different CO formation mechanisms are occurring, but depending on the temperature, one dominates over the other. This study illustrates the importance of the complex interplay of metal particles and oxidic support (at the interface), both actively participating in the CO₂ hydrogenation mechanism.

KEYWORDS: Ni_xMg_{1-x}O solid solution, CO₂ hydrogenation, methanation, metal–support interface, Ni catalysts



INTRODUCTION

CO₂ is at the central stage of global warming as changes in climate can be partially attributed to anthropogenic greenhouse gas emissions. In order to reduce its concentration in the atmosphere, one of the strategies considered is its activation and conversion. Currently, the use of CO₂ as a chemical feedstock is limited to only a few industrial processes like the synthesis of urea, polycarbonates, salicylic acid, and methanol, representing only a small fraction of the potential CO₂ available for conversion.¹ An effective way to reduce CO₂ emissions is to use it as a component for the fuel pool, which worldwide consumption is 2 orders of magnitude higher than that of chemicals.² The products of CO₂ hydrogenation such as hydrocarbons (e.g., CH₄) present the advantage that they can be stored and transported easily.³ For the methanation of carbon oxides, Ni has always been the catalytic material of choice, and this, since the very early studies of Paul Sabatier,⁴ because of its high activity and selectivity toward methane, and its relatively low price compared to the noble metals active in CO_x hydrogenation (Ru, Ir, Rh, and Pd).⁵

Many oxide supports have been investigated for Ni-based systems, and their properties were shown to have a large influence on the performances of the catalysts.⁶ However, most of the studies concentrate on the use of SiO₂ and Al₂O₃.

Although many experimental and theoretical studies have been carried out,^{5d,7} to date no consensus on the mechanism of the CO₂ methanation has been reached. Opinions diverge into two main hypotheses: the conversion of CO₂ to CO prior to methanation (CO is an intermediate) or the direct hydrogenation of CO₂ to CH₄ (CO is not an intermediate). In previous studies, MgO was used to provide an alternative reaction pathway (starting with the formation of Mg carbonate) and to minimize the production of CO through the inhibition of its desorption^{5d,7i} due to the strong basicity of the support as opposed to the usual SiO₂ or Al₂O₃.

Additionally, MgO shows great potential as NiO and MgO present the ability to form a solid solution, due to their very close ionic radii (about 0.02 Å difference).⁸ The strong interaction between the Ni species and the MgO, favors the formation of highly dispersed small Ni particles, enhancing the CO₂ conversion activity⁹ and stability.¹⁰ Paradoxically, the same interaction can lead to the reduction of the CO₂ methanation activity, because of the poor reducibility of the NiO–MgO solid solutions.^{10a}

Received: June 4, 2019

Revised: July 29, 2019

Published: August 6, 2019

As described above, the interaction between the Ni species and the MgO is the key factor for the optimization of the performances of Ni–Mg catalysts in CO₂ conversion reactions. The main factors that control this interaction are the choice of precursors,¹¹ the synthesis method,^{10b,12} and the calcination temperature.¹³ Among the different preparation methods, we choose to work with coprecipitation techniques that allow, with a proper adjustment of the precipitation parameters, the homogeneous distribution of the metal salts inside the catalysts precursors.¹⁴

The systematic variation of the calcination temperature of the Ni_xMg_{1-x}O precatalysts induces progressive changes of their chemical and structural properties, allowing the observation of correlations with their catalytic performances. The control of their reducibility means to control the dispersion of the Ni within Ni⁰/Ni_xMg_{1-x}O system and finally the adjustment of the metal vs support contribution. The structure–activity correlations drawn from this study participate to obtain a more complete picture of the reactivity of CO₂ conversion on supported catalysts.

■ EXPERIMENTAL METHODS

Synthesis. Ni_{0.1}Mg_{0.9}O solid-solution precatalyst was obtained by calcination of the phase pure hydroxy-solid-solution Ni_{0.1}Mg_{0.9}(OH)₂. This precursor was prepared by coprecipitation of the corresponding metal nitrates with ammonia, as previously reported.¹⁵ For this study, Ni_{0.1}Mg_{0.9}O samples (calcined at 400, 500, 600, 700, and 900 °C) were prepared, and are named after their Ni concentration and calcination temperature (e.g., Ni10_400 for Ni_{0.1}Mg_{0.9}O calcined at 400 °C). Reduced samples were named with the suffix “red” (e.g., Ni10_400red). Calcination was performed in a rotating oven with a rotation speed of 2 turns min⁻¹, under a synthetic air stream of 100 mL min⁻¹, and following a heating rate of 2 °C min⁻¹. The solids were held for 3 h at the final temperature, before cooling under the same gas flow.

XRD. X-ray diffraction (XRD) measurements were performed in Bragg–Brentano geometry on a Bruker AXS D8 Advance II theta/theta diffractometer, using Ni filtered Cu K α radiation and a position sensitive energy dispersive LynxEye silicon strip detector. The sample powder was filled into the recess of a cup-shaped sample holder, the surface of the powder bed being flush with the sample holder edge (front loading). The powder XRD data were analyzed using a full pattern fitting, according to the Rietveld method as implemented in the TOPAS software [TOPAS version 5, copyright 1999–2014 Bruker AXS].

TPR. Temperature-programmed reduction (TPR) of the samples was performed in a fixed bed reactor (quartz tube), in a 5% H₂ in Ar atmosphere, with a heating rate of 5 °C min⁻¹ to 1000 °C and were kept at this temperature for 1 h. The H₂ consumption was monitored with a thermal conductivity detector. The TCD detector was calibrated by reducing a known amount of CuO. Magnesium oxide supports present the large inconvenience of adsorbing very quickly, and very strongly, CO₂ and water from the atmosphere. As such, direct temperature-programmed reduction (TPR) leads to complex profiles, where the H₂ consumption peaks can correspond to interaction with the adsorbed species, or to actual reduction events. To avoid those interpretation problems and facilitate the peak attribution, all samples were preheated in argon before reduction, with a rate of 2 °C min⁻¹, to 500 °C, and hold at 500 °C for 1 h.

BET. Specific surface areas were determined by N₂ physisorption using the BET method¹⁶ in a Quantachrome Autosorb-1 machine. The samples were previously outgassed for 3.5 h at 80 °C.

TGMS. Thermogravimetric analysis (TG/DSC) was performed on a Netzsch STA449 Jupiter thermoanalyzer using 10 mg of sample placed into an alumina crucible (85 μ L) without lid. Evolution of the gas phase during reaction was monitored with a quadrupole mass spectrometer (Pfeiffer, QMS200 Omnistar). The thermal decomposition was performed from room temperature to 1000 °C, with a heating ramp of 2 °C min⁻¹ in a 21% O₂ in Ar atmosphere.

Ni Surface Area and Ni Particle Size Calculation. The metallic nickel surface area was determined by O₂ pulse thermal analysis.¹⁷ The samples were reduced inside a TG-MS setup and cooled to room temperature. Small amounts of O₂ were then pulsed onto the surface of the catalysts, oxidizing the metallic nickel particles. The amount of oxygen consumed during the oxidation was determined through the evolution of the mass of the catalyst (phenomenon also monitored by mass spectrometry) and the enthalpy of formation of the corresponding oxide was measured by differential thermal analysis to confirm the stoichiometry of the formed oxide. The Ni particle sizes are calculated using the following equations for the MCS (metal particle size).¹⁸

$$\text{MCS} = \frac{F}{(\text{Ni s.a.}_{\text{Ni}} d_{\text{Ni}})}$$

where Ni⁰ sa_{Ni} is calculated based on the measured Ni s.a. per weight, $F = 6$, shape factor for the assumption of spherical particles, and $d_{\text{Ni}} = 8.908 \text{ g cm}^{-3}$ density of metallic Ni particles.

SEM. The scanning electron microscopy (SEM) images were captured on an Hitachi S-4800 Field Emission Scanning Electron microscope working in the kV range 0.1 to 30.

STEM/TEM. Scanning transmission electron microscopy images (TEM, STEM, and EDX mapping) were captured on an aberration corrected TITAN 80-300 microscope operated at 300 kV. The sample preparation consisted of a dry deposition on a double tilt sample holder. Elemental analysis and mapping was obtained by using X-ray dispersive spectroscopy (EDX) also at 300 kV.

Catalytic Testing. The catalytic measurements were carried out in a fixed bed reactor consisting of a quartz U-tube, heated by a tube furnace (Carbolite). The reactor temperature is measured at the top of the catalyst bed. To avoid condensation of products (e.g., water), the reactors, part of the gas supply system, and the gas sampling system were placed in a heating closet that was kept at 100 °C. CO₂, H₂, and Ar were mixed outside of this closet via mass flow controllers (EL-FLOW, Bronkhorst). Gas analysis was performed online by a gas chromatography (gas chromatograph 6890A, Agilent) equipped with two channels. A thermal conductivity detector (TCD) was used to analyze CO₂, H₂, CO and Ar and a flame ionization detector (FID) was used to analyze CH₄. The precatalysts were reduced in situ as described previously and then systematically tested for the hydrogenation of CO₂ in a fixed gas mixture (60 mL/min, H₂:CO₂ 4:1, 20% Ar). Residual traces of C₂H₆ were monitored during testing. All carbon balance were greater than 97%. The reaction was carried out with MgO support only and did not show any conversion in the temperature range used (220–280 °C).

RESULTS AND DISCUSSION

Synthesis and Characterization of the Precatalyst. *Chemical Composition and Structure.* The concentration of Ni in the catalytic material is fixed to 10 at. %. A separated concentration series emphasized that catalysts with lower Ni loadings are hard to reduce and higher loadings lead to nonideal Ni distributions within the MgO lattice.¹⁵ The hydroxy precursor Ni10_(OH)₂ was obtained by controlled coprecipitation as previously reported.¹⁵ Thermogravimetric analysis was performed to understand the decomposition mechanism from the hydroxide to the oxide structure and is presented Figure 1.

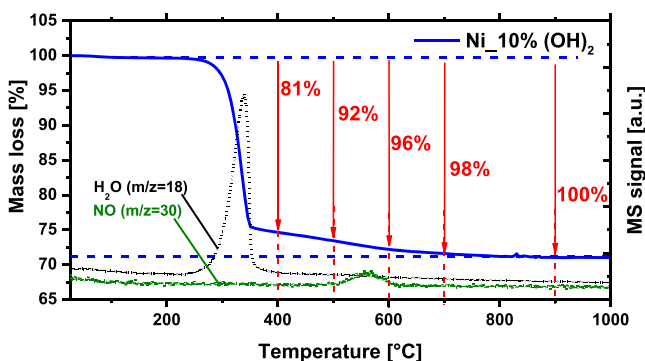


Figure 1. TG-MS analysis of Ni10_(OH)₂ with 2 °C min⁻¹ to 1000 °C in a 21% O₂ in Ar atmosphere. Mass loss (blue line) intensity of the MS signal (green for NO and for black for H₂O) and percentages of decomposition (red numbers).

The TG-MS analysis revealed one major thermic event between 200 and 380 °C, the main water loss (signal $m/z = 18$), corresponding to the transformation of the hydroxide structure to the oxidic one (decomposition stage 1). After 380 °C, the water signal shows a tail until 700 °C that corresponds to a much slower loss rate (decomposition stage 2). Additionally, at 500 °C, we observed a small signal ($m/z = 30$) corresponding to the release of NO, coming from the residual nitrates from the metal precursors used during synthesis.

Consequently, calcination temperatures lower than 400 °C were not investigated, as they would not be expected to form MgO but a phase mixture with the precursor.¹⁹ Five different

calcination temperatures were investigated, corresponding to 5 different percentages of decomposition of the hydroxide, going from 81 to 100%. Details of the calculations are presented in Table S1.

The hydroxide precursor has a brucite structure, while its decomposition product, MgO, has a periclase structure, both of which are represented in Figure S1. Full powder XRD patterns of both the precursor and the precatalysts (the calcination series) are presented Figure 2. Over the whole set of samples, no traces of the brucite precursor was found in the diffractograms of the calcined products even at the lowest calcination temperature (Ni10_400, see enlargement of Figure 2). Furthermore, we observe an increase in crystallinity with increasing calcination temperature.²⁰ The mechanism of the thermal decomposition of Mg(OH)₂ to MgO has been widely investigated over the past 50 years.²¹ The first stage of decomposition has been identified as the main structural, and compositional change from Mg(OH)₂ to MgO, while it appears that the residual water constituting the water-tail (decomposition stage 2, as seen Figure 1), only corresponds to the loss of chemisorbed water on the MgO planes. This agrees well with the absence of brucite traces in the XRD patterns, even for a calcination temperature of 400 °C.

Textural Properties. It is known that the decomposition of magnesium hydroxide involves a topotactic transformation,²² and as such there is a three-dimensional correspondence between the crystal structure of the precursors (Mg(OH)₂) and the final product (MgO). Indeed, the hexagonal close-packed structure of oxygen ions rearranges into a cubic close-packed structure without changing the macroscopic platelet-like structure of the material as seen Figures 3A,B and S1.

While increasing the calcination temperature from 400 to 600 °C, we observe a textural modification of the pellets (Figure 3B,C), as their surface becomes porous. Upon calcination the flakes of Mg(OH)₂ will hold together by overlap of the (001) surfaces and form buckled flakes aggregates of small MgO nanoparticles building blocks,²³ which kept irregular hollow channels that we can observe by TEM and through which the residual water can still escape^{23c,24} (Figure S2). Upon further calcination to 700 °C the porosity of the pellets becomes even more visible, but the external dimensions of the particles did not change, whereas at 900 °C morphological transformations can be observed. The previous pellet structure can still be

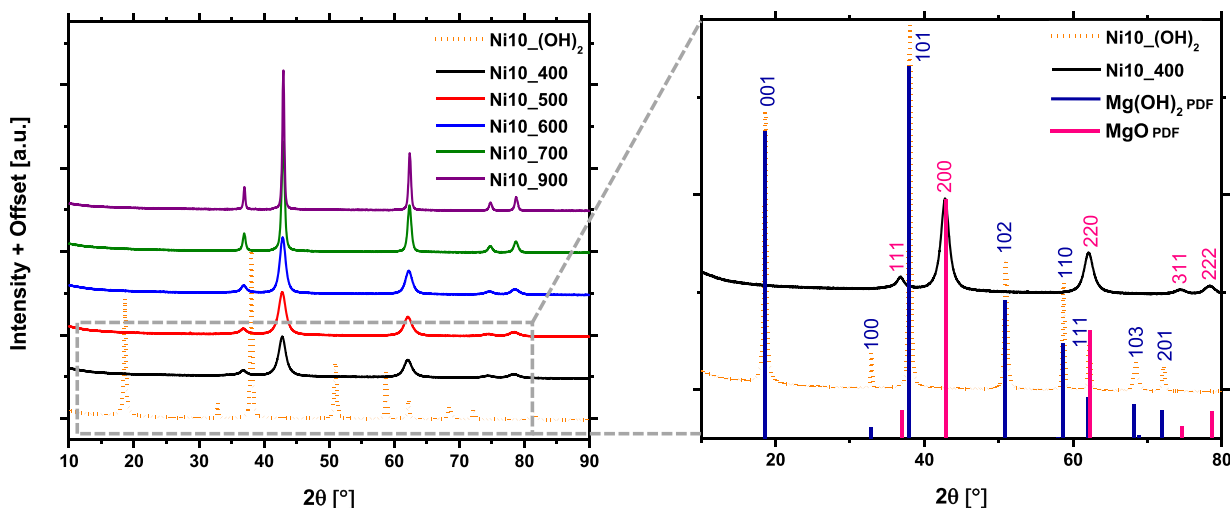


Figure 2. XRD patterns of the hydroxy precursor and of the calcination series and an enlargement on the Ni10_400 and Ni10_(OH)₂ patterns.

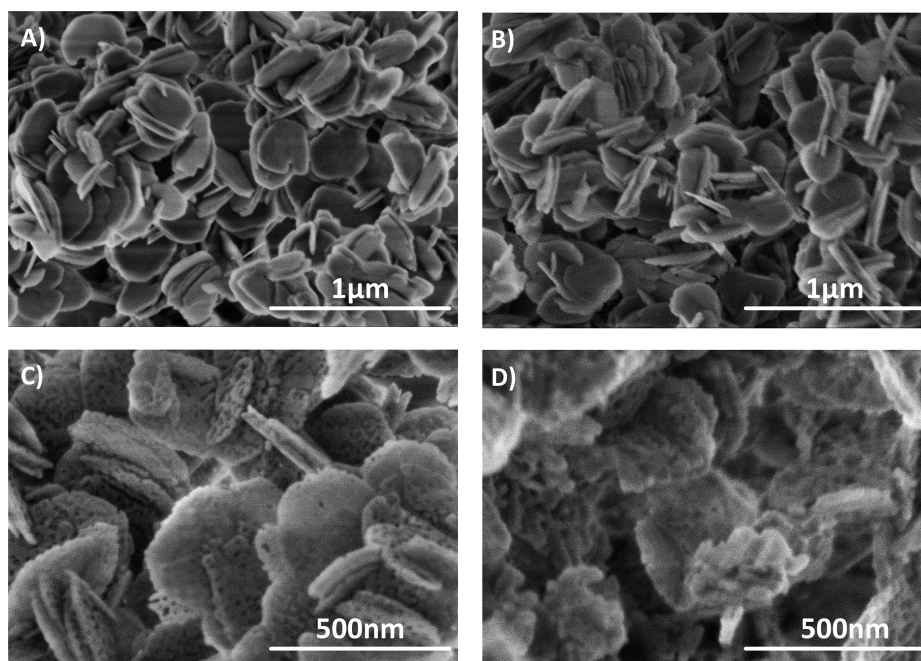


Figure 3. SEM images of (A) Ni10_(OH)₂, (B) Ni10_400, (C) Ni10_600, and (D) Ni10_900.

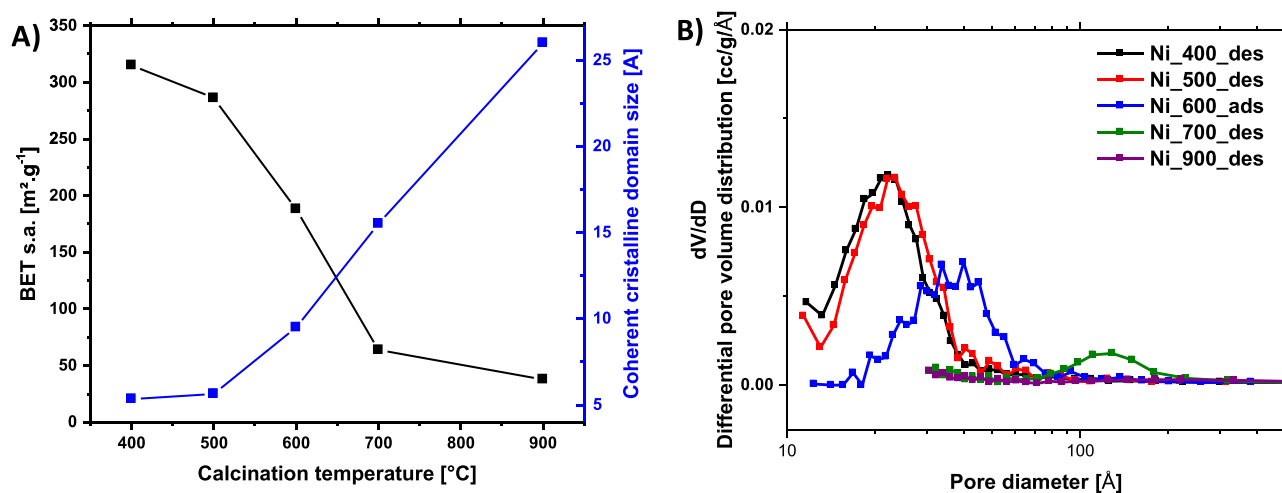


Figure 4. (A) Evolution of the specific surface area and the XRD crystallite size as a function of the calcination temperature and (B) differential pore volume distribution.

recognized, but most of the material seems to have agglomerated into shapeless aggregates (Figure 3D). The full SEM investigation can be found Figure S3. Elemental mapping was performed and revealed a very homogeneous distribution of the Ni inside the MgO pellets as shown Figure S4. The calcination temperature of the brucite precursors has a strong influence on the BET s.a. of the calcined material. As shown in Figure 4, the BET s.a. is decreasing with increasing calcination temperature, and its evolution follows the same trend as the materials' porosity. Between 400 and 500 °C, nearly no difference is observed in the pore volume, the pore diameter and the BET s.a. between 500, 600, and 700 °C a much larger decrease is observed in the BET s.a., showing a very good correlation with the decrease of the pore volume and the increase of the average pore diameter, indicating the loss of microporosity.

With an ongoing decomposition stage of the parent structure, larger pores are formed. The decrease in BET s.a. is in good correlation with the coherent crystalline size, attesting of the

unification of the crystallite domain.²⁵ Finally between 700 and 900 °C only very little change is seen in the BET s.a. as the composition of the sample remains unchanged (Figure 1), while morphological changes occurred (Figure 3D). We observe the final transition from a mesoporous to a nonporous material (Figure 4B), while the size of the coherent crystalline domains largely increases, evidencing a strong sintering phenomenon (Figure 4A).

While SEM images did not show any structural modification upon calcination,²⁶ the closing of the micropores by aggregation of the primary particles is evidenced by the above porosity study. All numerical values are shown Tables 1 and S2.

CHARACTERIZATION OF THE CATALYSTS

Reduction Behavior. All precatalysts were reduced in an atmosphere of 5% H₂ in Ar, with a heating rate of 5 °C/min until 1000 °C and a dwell time of 1 h, also prior to any catalytic

Table 1. Physical and Chemical Properties of the Prepared Samples

calcined samples			reduced samples		
ID	BET (m ² g ⁻¹)	reducibility (%)	BET (m ² g ⁻¹)	Ni s.a. (m ² g ⁻¹)	Ni PS (nm) ^a
Ni_400	315	74.5	72.9	6.41	7.9
Ni_500	286	64.2	77	6.31	6.9
Ni_600	188	58.8	80.42	6.35	6.3
Ni_700	63.7	19.1	57.6	2.39	5.4
Ni_900	37.7	18.1	27.2	2.41	5.1

^aCalculated Ni particle size, details see the [Experimental Methods](#)

evaluation. The reduction profiles obtained for the calcination temperature series are presented in [Figure 5A](#).

The samples Ni10_400 and Ni10_500 show two distinct H₂ consumption peaks, a sharp one at $T_1 = 320\text{--}350\text{ }^{\circ}\text{C}$ and a broader one centered around $T_2 = 740\text{ }^{\circ}\text{C}$, while all other samples only show a broad peak in the $740\text{--}800\text{ }^{\circ}\text{C}$ range.

According to the studies conducted on Ni_xMg_{1-x}O systems the reduction profiles in 5% H₂ in Ar show two specific peaks; one centered around $350\text{ }^{\circ}\text{C}$ corresponding to the reduction of Ni oxide aggregates, and a second one around $750\text{ }^{\circ}\text{C}$ corresponding to the reduction of the Ni inside the solid solution.²⁷ The use of simultaneous mass spectrometry revealed that the reduction profiles seem, at first sight, to perfectly match the predicted reduction events. However, for this system the peak at $350\text{ }^{\circ}\text{C}$ does not correspond to any water release in the MS spectrum (as seen [Figure 5B](#)), the inevitable byproduct of the NiO reduction ([eq 1](#)).



The first reduction event corresponds to the release of nitrogen ($m/z = 28$) from the reduction of the residual nitrates, used as precursor salts (Mg(NO₃)₂·6(H₂O) and Ni(NO₃)₂·6(H₂O)). Their presence could be confirmed by TG-MS analysis, as seen in [Figure 1](#) (event between 500 and $600\text{ }^{\circ}\text{C}$). Additionally, we observed through the evolution of the TPR profile as a function of the calcination temperature ([Figure 5A](#)) that the peak centered at $350\text{ }^{\circ}\text{C}$ is decreasing between Ni10_400 and Ni10_500 and finally disappears for the

Ni10_600 sample, as all of the residual nitrates were already released during the calcination. As a consequence, we observe only a single reduction peak ($T_2 = 740\text{ }^{\circ}\text{C}$) corresponding to the reduction of Ni embedded in the MgO structure, and no signal corresponding to Ni aggregates.

With increasing calcination temperatures, the reducibility of the samples decreases (decreasing area under the TPR profiles). This phenomenon is in accordance with the literature, and attributed to the progressive transformation of the free Ni particles on MgO, into a Ni-rich surface NiO-MgO solid solution, and in a second consecutive step, to the diffusion of the Ni atoms deeper inside the MgO to form an ideal solid-solution.^{13b,27a,c,28} With increasing calcination temperatures, the homogeneous distribution of the Ni atoms inside the MgO bulk hinders their reduction. However, as seen earlier, based on our already established synthesis protocol,¹⁵ we already have an ideal solid-solution even at the lowest calcination temperatures ([Figure 5A](#)) and the Ni²⁺ diffusion cannot fully explain the decrease of reducibility observed (primary calcination effect).

As we can see [Figure 6A](#) the reducibility of the samples seems to correlate with the evolution of the BET surface area (BET s.a.), suggesting a possible link between the two parameters (details in [Table 1](#)). High temperature treatment reduces largely the surface area of the samples, influencing the accessibility of the Ni. A large amount of Ni is trapped inside the larger oxidic particles (without micropores $700\text{ }^{\circ}\text{C}$ /mesopores $900\text{ }^{\circ}\text{C}$, in contrast to the lower calcination temperature) lowering the contact area between the reductive gas and the material (secondary calcination effect).

Characterization of the Metallic Ni. The Ni metallic surface area was determined for each sample using O₂ pulse thermal analysis as reported earlier.¹⁷ Its evolution as a function of the calcination temperature is shown [Figure 6B](#) and mainly follows the reducibility of the samples, which is self-controlled by the specific surface area of the calcined samples.

The full patterns and the corresponding Rietveld analysis of the reduced samples are shown in [Figure 7](#). TPR experiments show that the reducibility within the sample series largely decreased with increasing calcination temperatures. A phenomenon that was also observed by XRD analysis of the reduced samples. Indeed, the intensities of the diffraction peaks

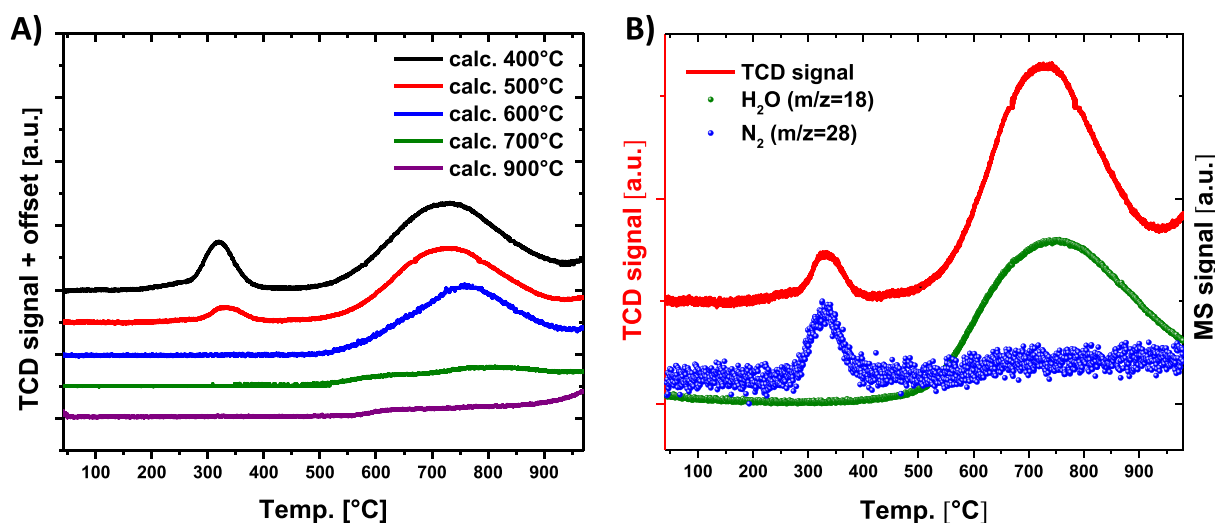


Figure 5. (A) Superposition of the reduction profiles of the calcination series conducted in 5% H₂ in Ar. (B) Reduction profile of the Ni10_500 °C sample with simultaneous MS analysis.

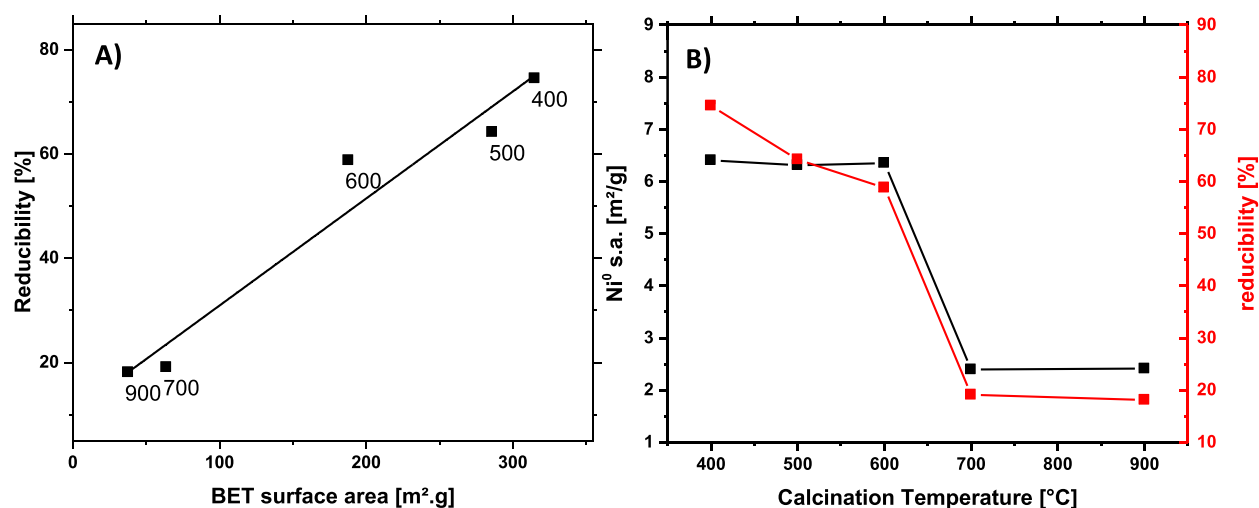


Figure 6. (A) Reducibility of the initial Ni as a function of the BET s.a. (with calcination temperature in °C as label). (B) Ni⁰ s.a. and reducibility as a function of the calcination temperature.

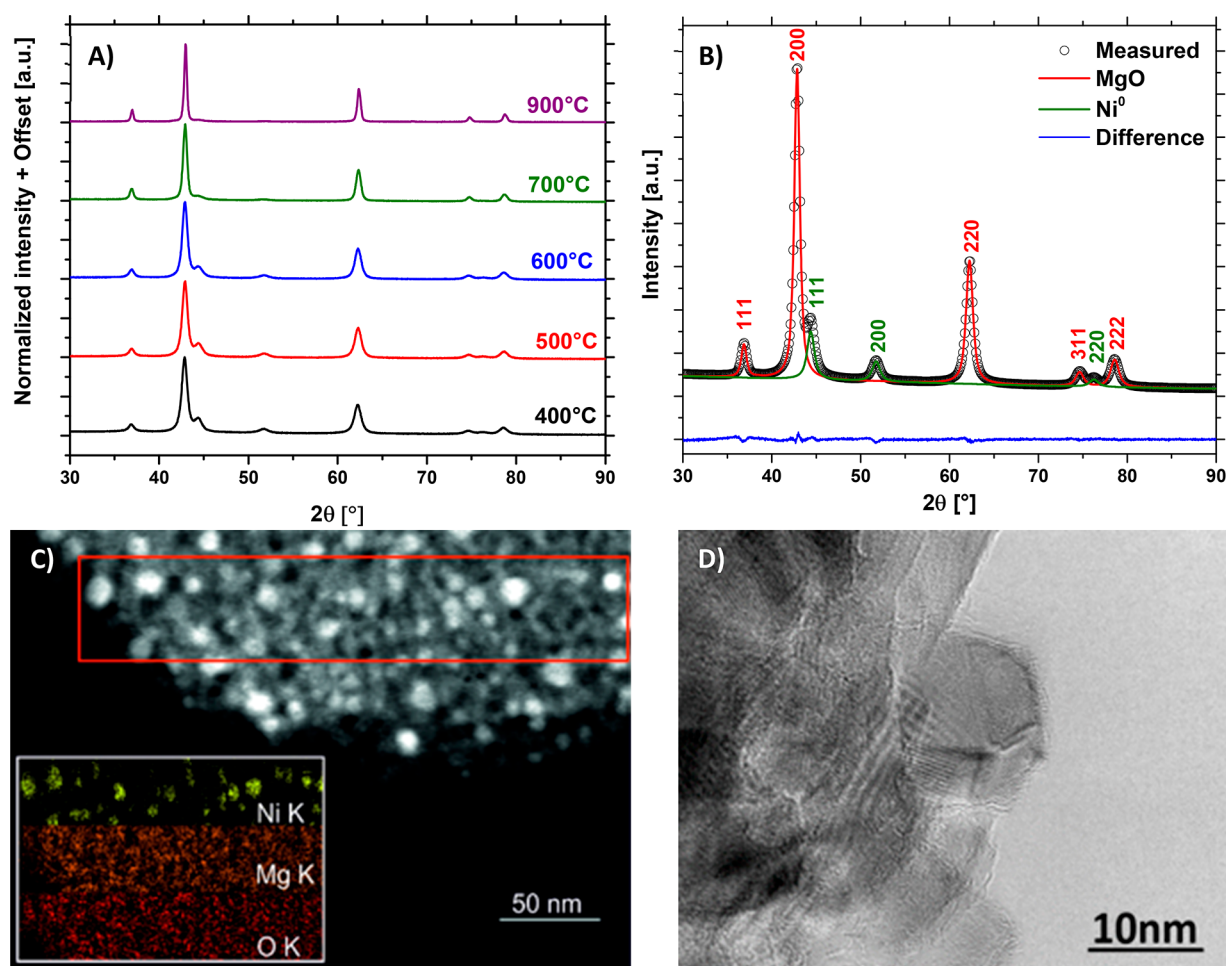


Figure 7. (A) Superposition of all the XRD patterns of the reduced samples. (B) Rietveld fit of Ni10_400red with the measured (black), calculated (red line for MgO and green line for Ni⁰) diffraction patterns and the corresponding difference curve (blue). (C) STEM image of Ni10_400red with the elemental mapping of the red area. (D) HR-TEM of a Ni particle from Ni10_600.

corresponding to metallic Ni ($2\theta = 44.3$, 51.6 , and 76.1) are clearly decreasing with increasing calcination temperature, while their width is enlarged (characteristic of smaller crystallite domains). Furthermore, the theoretical Rietveld fit of Ni10_400red calculated for MgO (red line) and Ni⁰ (green

line) agrees perfectly with the experiment (black circles). We detect only tiny deviation in the difference curve (blue line).

The Ni10_400red sample was analyzed by transmission electron microscopy (TEM) without any contact to the air. After reduction we obtain a very crystalline material, crystallizing as

numerous little cubes (Figure S5). The dark field image Figure 7C allows, due to the high contrasting, a clear differentiation between the metallic Ni particles (bright spots) and the MgO support, which was confirmed by elemental mapping. The Ni particles (~ 10 nm) appear to be very homogeneously dispersed, as evidenced by high resolution (S)TEM images (Figures 7C and S12 A,C,D). Nearby well faceted Ni particles (Figure S6) also some partly Wulff-constructed Ni particles are identified (e.g., Figure 7D). Generally, the Ni particles are well separated from each other and are embedded/stabilized in the oxidic support. Further, the Ni particles seem not to be covered by the poorly reducible $\text{Mg}_{1-x}\text{Ni}_x\text{O}$ support, which is confirmed by integral surface titration experiments.¹⁷

Textural Properties. The evolution of the BET s.a. after reduction shows, contrarily to the calcined samples, a volcano profile (Figure 8) which can be explained by the different

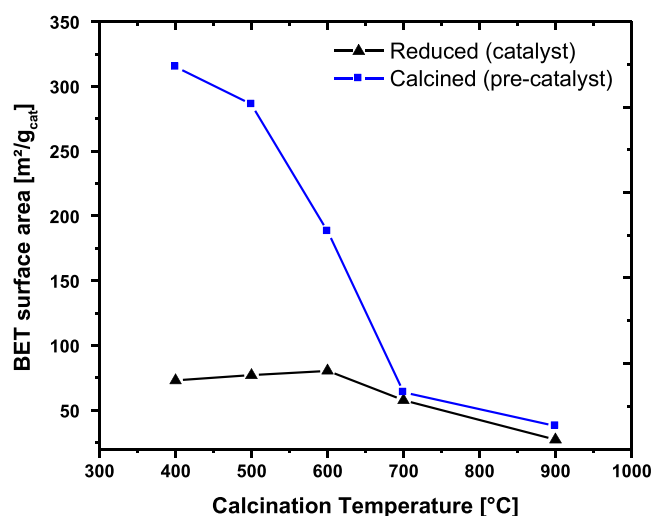


Figure 8. Evolution of the BET surface area of the calcined samples compared to the reduced sample as a function of the calcination temperature.

stability of the various types of pores present before reduction. Comparison between the Ni10_400red and Ni10_600red shows that the smaller the micropores, the stronger the collapse of the specific surface area. Furthermore, it seems that only the micropores were destroyed by the reductive treatment, as for Ni10_700 (largest pores) and Ni10_900 (nonporous) the BET s.a. stays almost unaffected. This might be explained by the consumption of lattice oxygen coupled to Ni (formation of H_2O and Ni metal particles), which leads to a loss of the microporous structures. The higher the BET s.a. area of the precatalyst was, the higher is the degree of reduction and stronger pronounced is the loss of the resulting BET s.a. of the catalyst. Further, this structural adaption is coupled to the quantity of metallic Ni forcing the reduction process autocatalytically (more Ni, more activated H_2 etc.), finally leading to the volcano-type profile of the reduced catalysts (Figure 8).

CATALYTIC TESTING

The temperature range for the testing was chosen between 220 and 280 °C. The lower limit was chosen to avoid the formation of $\text{Ni}(\text{CO})_4$ ²⁹ and the upper limit to keep the conversion of CO_2 below 10%, in order to work in the kinetic regime (Figure S7). The calcination series was tested for the methanation of CO_2 . For all samples, the CO_2 conversion is increasing with increasing

temperature as seen Figure 9A. Each measurement point corresponds to the average of 8 h of measurement (error bars smaller than the symbols), during which negligible deactivation was observed (Figure S8). The Ni10_600 sample (presenting the highest activity) was chosen for a more detailed investigation. The stability of the catalyst was verified by testing at the same conditions following an increasing and then decreasing temperature ramp, as illustrated (Figure S9). The experiment shows a very good reproducibility with identical reaction rates at the same temperatures. The same catalyst was tested at high conversion near the equilibrium (405 °C, 70% conversion) for more than 100 h time on stream. After this long-time high performance experiment no deactivation was observed in the low-temperature regime. Besides, structural analysis by XRD and TEM analysis before and after catalysis did not reveal any change in the $\text{Mg}_{1-x}\text{Ni}_x\text{O}$ support or the metallic Ni, demonstrating the relevance and suitability of the chosen $\text{Ni}^0/\text{Mg}_{1-x}\text{Ni}_x\text{O}$ system for this investigation. All catalytic results, XRD analysis and TEM particle size distributions are presented in the Supporting Information (Figures S10, S11, and S12 and Table S3). The long time stability (~ 80 h at each temperature) of the catalysts was also investigated and revealed that again a negligible deactivation was observed (Figure S13 and Table S4). All samples were mainly selective toward CH_4 (Figure S14). Ni10_900 however shows large differences with the other samples in terms of reactivity and selectivity, in good agreement with the results discussed above, which already identified this sample as the outlier of the series (i.e., with respect to morphology, porosity, crystalline domain size, and reducibility). In Figure 9B the reaction rates at 280 °C were plotted as a function of the calcination temperatures. The CO_2 conversion revealed a volcano profile with a maximum at 600 °C. All other testing temperatures presented the same profile and are shown in the Supporting Information together with a selectivity-conversion plot of the entire series of catalysts (Figure S16 and S17). Since the Ni particle size (PS) is an important issue with respect to its influence on the catalysts' performances (activity and selectivity), the Ni PS was calculated (Figure 9C, see also Table 1). With increasing calcination temperature, the Ni PS decreases incrementally and follows the trend of the BET s.a. of the precatalysts (Figure S15). This is again in very good agreement with the findings above emphasizing a crucial role of the calcination conditions on the materials properties. Figure 9D shows the selectivity values to CH_4 at 280 °C (extracted from Figure S14). The activity profiles (between 220 and 280 °C) follow always a volcano-type behavior with respect to the calcination temperature (Figures S8 and S16) and show no correlation with the Ni PS (Figure 9C). In addition, the selectivity values to CH_4 (Figures S14 and 9D) show no pronounced correlation between each other, strongly evidencing no correlation of the Ni PS and the catalytic performance (since selectivity and CO_2 conversion values are free of any normalization effects). The absence of a Ni PS effect indicates an important role of the residual $\text{Ni}_x\text{Mg}_{1-x}\text{O}$ support and its interfacial contact to the Ni metal particle, which is obviously mainly affected by the calcination temperature.

The formation rates of each product were plotted for each sample and at each testing temperature (Figures 10A–D and S18). At 220 °C both the CH_4 and the CO formation rates show a volcano profile (Figure 10A,B), while at 280 °C large differences are visible between the two product rates (Figure 10C,D). The CH_4 formation rate still follows a volcano profile, while the CO formation rate seems to indicate a two-plateau

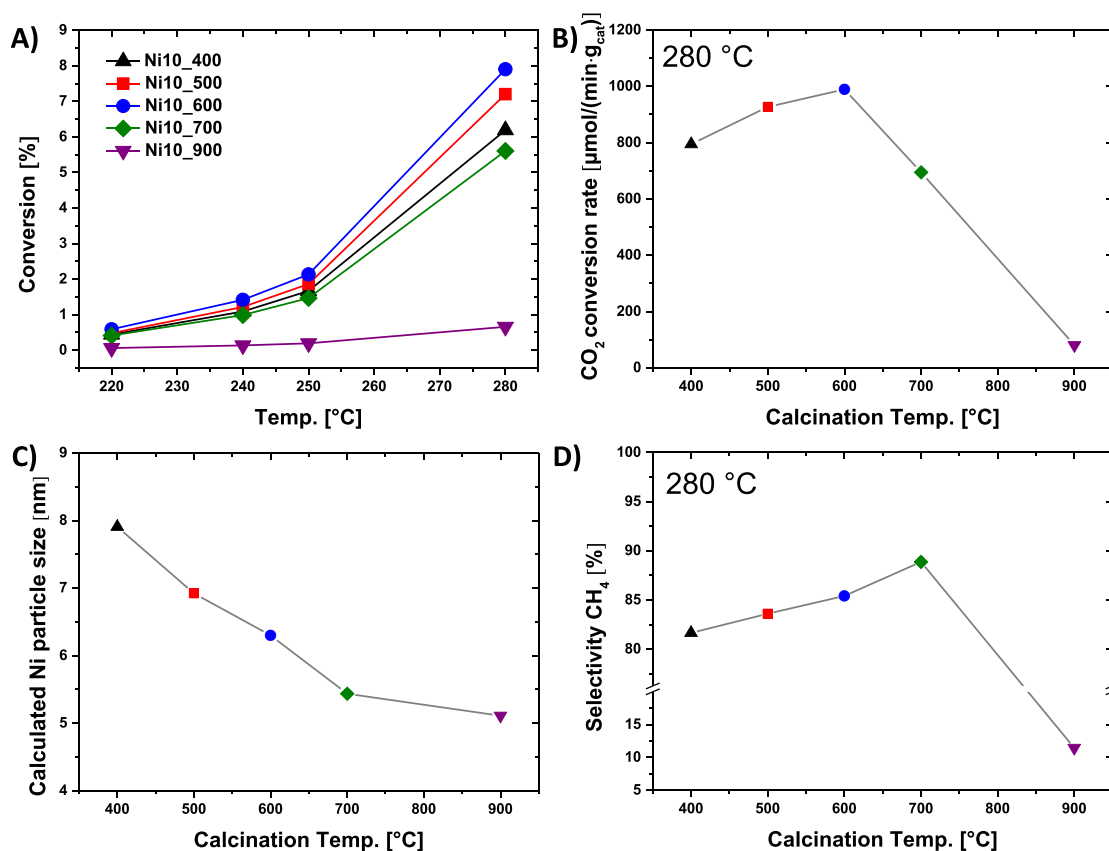


Figure 9. (A) CO₂ conversion as a function of the testing temperature in %. (B) CO₂ conversion rate at 280 °C as a function of the calcination temperature of the Ni 10 sample. (C) Calculated Ni particle size as a function of the calcination temperature. (D) Selectivity to CH₄ at 280 °C testing temperature plotted vs the calcination temperature.

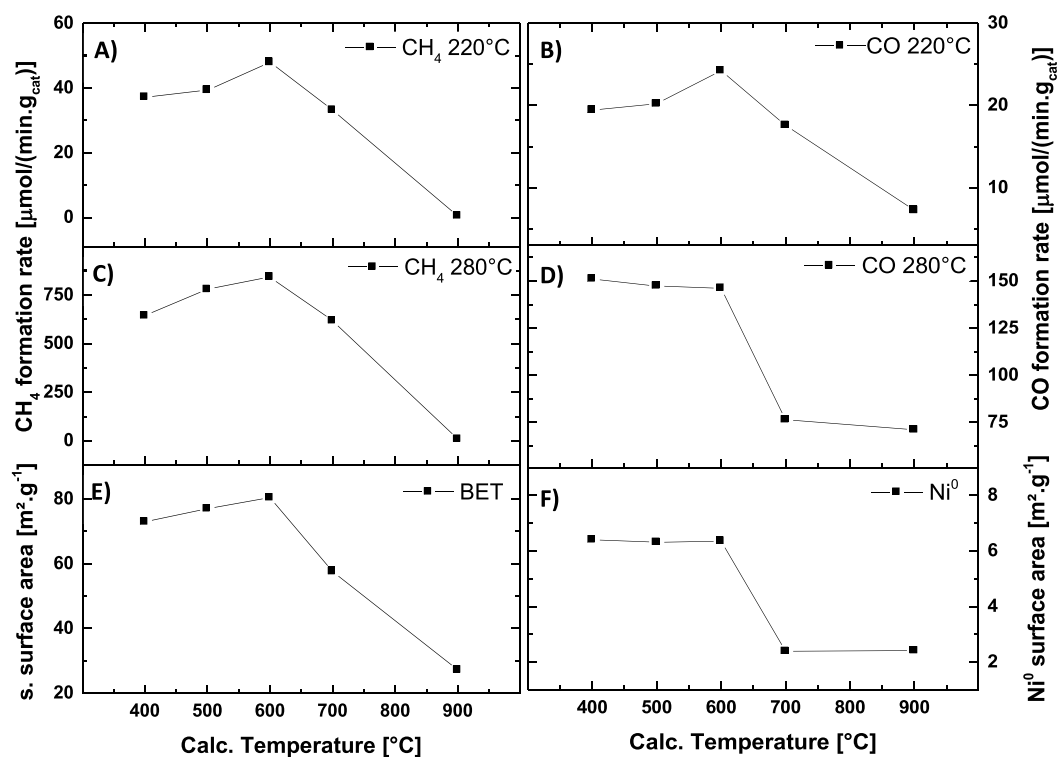


Figure 10. Formation rates of (A) CH₄ at 220 °C, (B) CO at 220 °C, (C) CH₄ at 280 °C, (D) CO at 280 °C, (E) BET specific surface area, and (F) Ni⁰ surface area as a function of the calcination temperature.

profile. The change in the profiles of the reaction rates for CO corresponds to a reversible and stepwise process controlled by the reaction temperature (Figures S18 and S9B).

When comparing those profiles to the physical properties of the calcination series, it becomes clear that we observe a direct correlation between the CH₄ and CO formation at 220 °C and the BET s.a., whereas at 280 °C, when the CH₄ formation still shows a very good correlation with the BET s.a., the CO formation rate shows the same peculiar profile as the Ni⁰ surface area. All correlations between the product formation rates and the physical properties of the samples were analyzed and are presented in Figure S19. Consequently, plotting the identified correlations (Figure S19) as normalized reactions rates (Figure S20A,B) very similar values at different calcination temperatures are gained (as expected for comparable catalysts), excluding the CH₄ rates for the Ni₁₀_900 catalyst. This matches, however, perfectly with results above, discussing the outlying character of the sample calcined at 900 °C with respect to structural and catalytic properties. Product formation rates give mainly information about the rate-determining step of the reaction, which does not seem to change for CH₄ at different temperatures but which appears to be sensitive to the reaction temperature when it comes to the formation of CO. This change appearing between 250 and 280 °C was also observed in the Arrhenius plot of the CO₂ conversion rate between 265 and 270 °C (Figure 11), revealing a higher apparent activation energy ($E_a = 116.7$ vs 95.9 kJ mol⁻¹) at higher temperature.²⁹

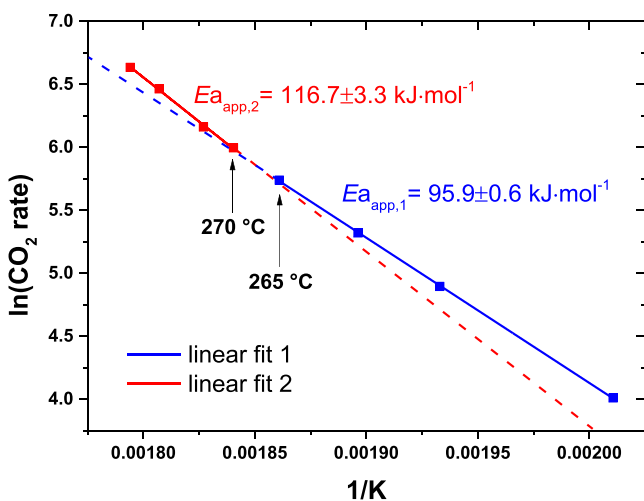


Figure 11. Arrhenius plot of the Ni₁₀_600 sample over the whole temperature range for the CO₂ conversion.

The E_a for both products was also determined and revealed that the E_a associated with the CH₄ formation is significantly higher than the one of the CO formation (123–106 vs 91–71 kJ mol⁻¹) as shown in Figure S21.

The reaction orders of CH₄ and CO with respect to H₂ and CO₂ were determined both before and after this “transition” temperature (at 220 and 280 °C) and are shown in Figure 12A–D. The determined uncertainties correspond to the estimated standard deviation. As already indicated by the identical profiles of the CH₄ formation rates at various temperatures, the CH₄ reaction orders are almost unaffected by the temperature (220 and 280 °C, Figure 12A,B). The small reaction order of $n_{\text{CH}_4}(\text{CO}_2) \approx 0.1$ shows that the CH₄ reaction rate is hardly dependent on the $p(\text{CO}_2)$, which means within a Langmuir–

Hinshelwood analog mechanism a strong binding of the adsorbent/intermediate (high coverage of sites already at low partial pressures). The reaction order of $n_{\text{CH}_4}(\text{H}_2) = 0.46$ –0.48 shows a strong dependence on the $p(\text{H}_2)$. Since the CH₄ reaction rates correlate with the BET s.a. and the activation of H₂ occurs very likely on Ni, the relevant reaction sites are probably located at the perimeter/interface of the Ni metal and Ni_xMg_{1-x}O support. As a consequence the rate-determining step is interpreted as hydrogen induced conversion of this interfacial intermediate. This is in line with our recent study on Ni single atoms and clusters,¹⁵ where surface formate species (as possible relevant intermediates) were identified by in situ IR at the metal/metal oxide interface. The reaction orders of CO are different at 220 and 280 °C, which fit perfectly to the change in the profile of the reaction rates (Figure 12C and D). The $n_{\text{CO}}(\text{H}_2) = 0.19$ –0.34 is rather small compared to the $n_{\text{CO}}(\text{CO}_2) = 0.57$ –0.67 (and vice versa with respect to n_{CH_4}).

The temperature dependent change of the CO reaction rates might be explained by a series of TPD experiments. To mimic the stability of CO₂-derived adsorbates on the Ni_{0.1}Mg_{0.9}O support, the unreduced precatalyst (calcined at 600 °C) is heated in syn air (21% O₂ in Ar) and H₂ (5% in Ar) after feed contact (Figure 13A). Progressive heating revealed that in a reducing atmosphere only the reaction product CO ($m/z = 28$) are visible. The desorption temperature is in the range where the CO reaction rates change its profile. Heating in oxygen containing atmosphere shows only CO₂ as desorbing species from the surface. Peak deconvolution of the CO₂ desorption profile shows three main events of desorption (Figure S22). Reference experiments with pure MgO identify the second desorption feature as related to MgO (Figure S23, here under H₂ atmosphere no product formation occurred). The first desorption feature might be related to Ni sites as part of the Ni_xMg_{1-x}O (decreased CO₂ adsorption energies)^{15,30} and the third event to under-coordinated metal sites (increased adsorption energies of CO₂).¹⁵ Since the CO rates correlate at e.g. 220 °C with the available BET s.a., CO₂ is adsorbed/stabilized (Figure 13A) on the surface of the Ni_xMg_{1-x}O support and the rates are strongly dependent on the $p(\text{CO}_2)$. At 280 °C, CO₂ and related intermediates desorb from the surface (Figure S22, event 3) and the CO rates correlate with the Ni⁰ surface area. We interpret these findings as strong evidence for a change of the rate-determining step, where the dissociative CO₂ activation on Ni⁰ becomes dominant and the reaction orders change accordingly (decrease of the surface binding strength of CO₂ or a related intermediate, increase of $n_{\text{CO}}(\text{CO}_2)$ from 0.57 to 0.67). The CO rates at 280 °C are almost unaffected by the $p(\text{H}_2)$, interpreted as a direct transfer of activated hydrogen on the Ni surface (which should sufficiently be available independent from the $p(\text{H}_2)$). The hydrogen transfer at 220 °C is possibly realized from Ni atoms and clusters on the Ni_xMg_{1-x}O support which is able to activate H₂ dissociatively (adsorption energies -90 kJ/mol).¹⁵ The involvement of hydrogen spillover or diffusion processes are not excluded, but at this point rather speculative and beyond the scope of this manuscript. Since we discussed in the TPD experiments unreduced precatalyst, no conclusion on the CH₄ rates is possible (no metal/metal oxide interface). However, our findings are supported by determining the apparent E_a for CO and CH₄ in the low temperature regime (220–275 °C) for the calcination series (Figure 13B,C). The E_a for CO decreases incrementally with increasing calcination temperature (Figure 13B) indicating the favored Ni-enriched Ni_xMg_{1-x}O support

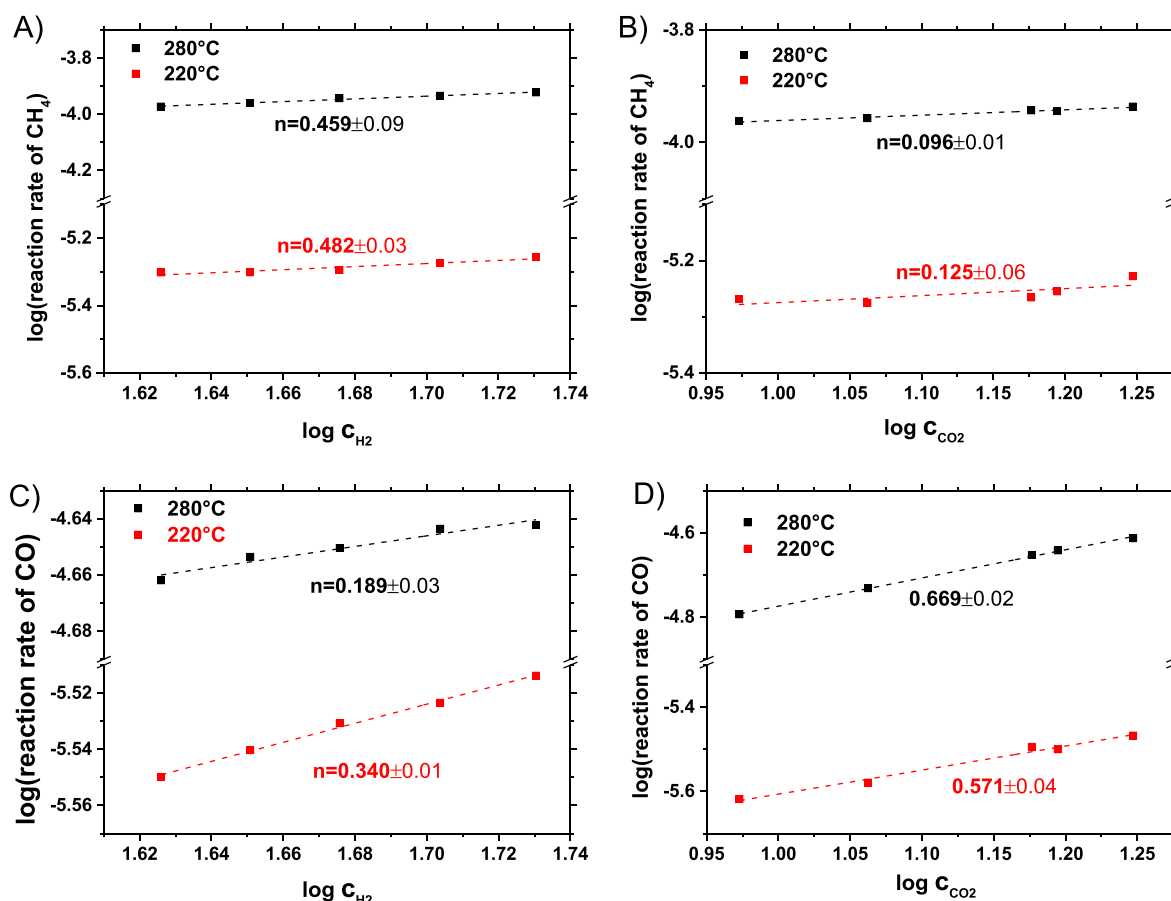


Figure 12. Reaction order n at 220 and 280 °C. (A) CH_4 formation with respect to c_{H_2} and (B) c_{CO_2} . CO formation as a function of the (C) c_{H_2} and (D) c_{CO_2} .

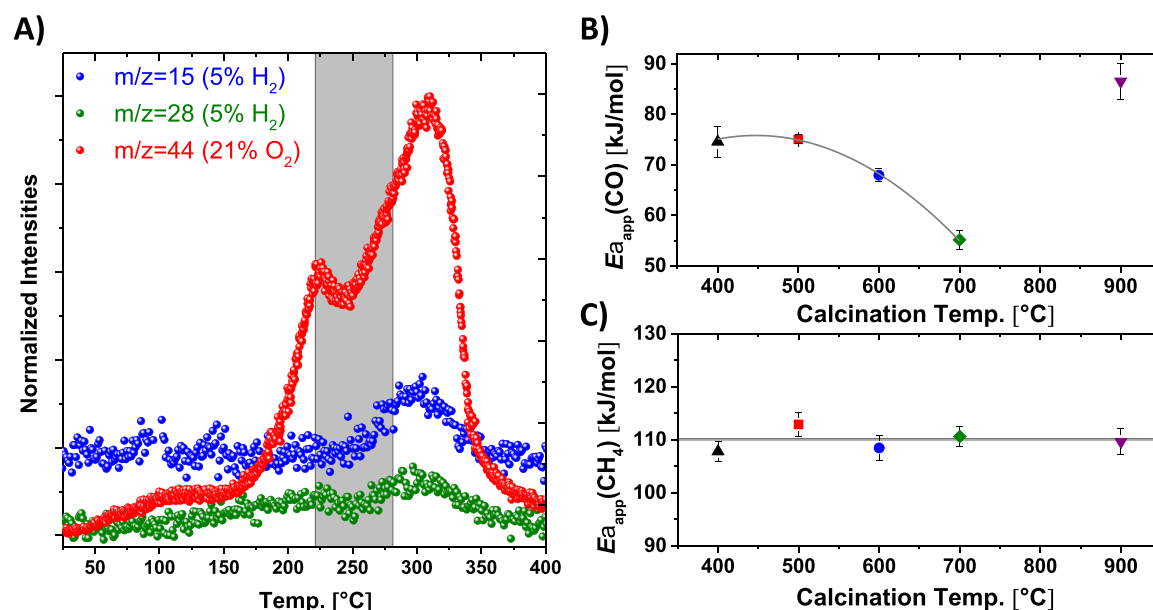


Figure 13. (A) Desorption experiments of Ni₁₀₆₀₀ in different atmospheres, gray column symbols the relevant temperature range of 220–280 °C. Apparent activation energies determined between 220 and 275 °C of (B) CO and (C) CH_4 for the calcination series.

(see reducibility Figure 6B). The metal/metal oxide interface should be mainly unaffected from the calcination temperature (identical reduction treatment at 1000 °C) and indeed the E_{a} for CH_4 are almost identical (Figure 13C). The formation of CH_4 from a consecutive reaction of the CO formation as dominant

path is very unlikely since increasing the contact times led also to an increase of the CO and CH_4 rates (decoupled mechanism) and not to a decrease of the CO rates (Figure S24); however, a detailed mechanistic clarification is also beyond the scope of this manuscript.

■ FINAL DISCUSSION AND CONCLUSION

In the present work, a series of catalysts prepared at different calcination temperature is investigated. The calcination temperature mainly affects the porosity, available BET s.a. and reducibility of the catalysts with consequences on the catalytic performance in the CO₂ hydrogenation. The Ni particles sizes are predetermined by the reducibility of the samples, which is in turn a function of the calcination temperature. All samples are reduced under identical conditions (much higher than calcination temperature), leading to strongly embedded/stabilized Ni particles by the Ni_xMg_{1-x}O support. This interpretation is supported by stability tests, where no deactivation was observed even after testing near the equilibrium for extended time on stream (more than 120 h). The narrow particle size distribution and XRD profiles did not change even after high performance testing, evidencing the high stability of the support stabilized and well faceted Ni particles. The most active sample (Ni10_600) was kinetically analyzed in detail. A change of the apparent activation energy was observed for the CO₂ conversion in different temperature regimes. This feature is usually attributed to simultaneous and competing reactions or reaction mechanisms to which different activation energies are associated.³¹ This matches perfectly with the changes of the formation rate profiles (rate-determining step) observed for the CO formation. The stable dependency of the CH₄ rates evidence a product formation following the same rate-determining step, respectively. This identifies the CO formation as origin of the change in the E_a at higher temperatures. The change in apparent activation energy would in this case reflect two competing reactions, involving different active sites, relevant in different temperature regimes. The first one, limited by the activation of CO₂ and related intermediates on the basic Ni_xMg_{1-x}O support, only relevant at low temperatures as the CO₂-derived intermediates (e.g., formate) become instable at higher testing temperatures. The second one limited by phenomena directly involving the metallic Ni surface area. These findings are supported by the reaction orders which identify the $p(\text{CO}_2)$ as strongly CO rate influencing and a minor impact of $p(\text{H}_2)$, particularly at elevated temperatures. Interestingly, those different reaction sites relevant in different temperature regimes were both proposed separately in the literature. On various systems, mechanisms were claimed in which CO₂ activation occurred either on the oxidic support or dissociatively on the metallic Ni.^{5d,7g,i,32} In our study it appears that both proposed hypothesis take place, dependent on the catalyst (its basicity) and the chosen conditions.

Since the H₂ activation happens very likely on the metallic Ni and the reaction rates correlate with the BET s.a., the distance of the CO₂-derived adsorbate (e.g., formate) to the metallic Ni particles might be a descriptor for selectivity toward CH₄ (adsorbing directly at the interface favors CH₄). The CH₄ rates correlate independent of the reaction temperature with the BET s.a. strongly influenced by the $p(\text{H}_2)$. This implies an identical rate-determining step probably involving a hydrogenation step of a CO₂ derived intermediate like formate. The characterization of the catalysts and the kinetic evaluation serve as example on the importance of the complex interfacial interplay between metal and support, in which also the support (here: Mg_{1-x}Ni_xO) actively participates in the CO₂ hydrogenation reaction network.

■ ASSOCIATED CONTENT

Supporting Information

The Supporting Information is available free of charge on the ACS Publications website at DOI: 10.1021/acscatal.9b02332.

Detailed descriptions of the conducted experiments, on the applied electron microscopy, the materials characterization, the kinetic evaluation, and analysis of the spent catalysts (PDF)

■ AUTHOR INFORMATION

Corresponding Author

*E-mail: efrei@fhi-berlin.mpg.de.

ORCID

Elias Frei: 0000-0003-3565-1199

Notes

The authors declare no competing financial interest.

■ ACKNOWLEDGMENTS

The authors thank W. Frandsen for the SEM images, J. Plagemann and M. Hashagen for BET analysis, and J. Allan for TGMS measurements. M.-M.M. thanks Unicat for financial support, "Förderkennzeichen EXC 314/1 UNICAT".

■ REFERENCES

- (1) Quadrelli, E. A.; Centi, G.; Duplan, J.-L.; Perathoner, S. Carbon Dioxide Recycling: Emerging Large-Scale Technologies with Industrial Potential. *ChemSusChem* **2011**, 4 (9), 1194–1215.
- (2) Centi, G.; Perathoner, S. *Green Carbon Dioxide: Advances in CO₂ Utilization*; John Wiley & Sons: New York, 2014; p 322.
- (3) Götz, M.; Lefebvre, J.; Mörs, F.; McDaniel Koch, A.; Graf, F.; Bajohr, S.; Reimert, R.; Kolb, T. Renewable Power-to-Gas: A technological and economic review. *Renewable Energy* **2016**, 85, 1371–1390.
- (4) Sabatier, P.; Senderens, J. B. *Acad. Sci. Paris*. **1902**, 134 (1), 514–689.
- (5) (a) Fischer, F.; Tropsch, H. Über die direkte Synthese von Erdöl-Kohlenwasserstoffen bei gewöhnlichem Druck. (Erste Mitteilung). *Ber. Dtsch. Chem. Ges. B* **1926**, 59 (4), 830–831. (b) Fischer, F.; Tropsch, H.; Dilethy, P. *Brennst. Chem.* **1925**, 6, 265. (c) Hou, Z.; Yokota, O.; Tanaka, T.; Yashima, T. Surface properties of a coke-free Sn doped nickel catalyst for the CO₂ reforming of methane. *Appl. Surf. Sci.* **2004**, 233 (1–4), 58–68. (d) Park, J.-N.; McFarland, E. W. A highly dispersed Pd–Mg/SiO₂ catalyst active for methanation of CO₂. *J. Catal.* **2009**, 266 (1), 92–97.
- (6) Rönsch, S.; Schneider, J.; Matthischke, S.; Schlüter, M.; Götz, M.; Lefebvre, J.; Prabhakaran, P.; Bajohr, S. Review on methanation – From fundamentals to current projects. *Fuel* **2016**, 166, 276–296.
- (7) (a) Dreyer, J. A. H.; Li, P.; Zhang, L.; Beh, G. K.; Zhang, R.; Sit, P. H. L.; Teoh, W. Y. Influence of the oxide support reducibility on the CO₂ methanation over Ru-based catalysts. *Appl. Catal., B* **2017**, 219, 715–726. (b) Pan, Q.; Peng, J.; Wang, S.; Wang, S. In situ FTIR spectroscopic study of the CO₂ methanation mechanism on Ni/Ce_{0.5}Zr_{0.5}O₂. *Catal. Sci. Technol.* **2014**, 4 (2), 502–509. (c) Vesselli, E.; De Rogatis, L.; Ding, X.; Baraldi, A.; Savio, L.; Vattuone, L.; Rocca, M.; Fornasiero, P.; Peressi, M.; Baldereschi, A.; Rosei, R.; Comelli, G. Carbon Dioxide Hydrogenation on Ni(110). *J. Am. Chem. Soc.* **2008**, 130 (34), 11417–11422. (d) Falconer, J. L.; Zagli, A. E. Adsorption and methanation of carbon dioxide on a nickel/silica catalyst. *J. Catal.* **1980**, 62, 280. (e) Ibraeva, Z. A.; Nekrasov, N. V.; Gudkov, B. S.; Yakerson, V. I.; Beisembayeva, Z. T.; Golosman, E. Z.; Kiperman, S. L. Kinetics of methanation of carbon dioxide on a nickel catalyst. *Theor. Exp. Chem.* **1991**, 26 (5), 584–588. (f) Heine, C.; Lechner, B. A. J.; Bluhm, H.; Salmeron, M. Recycling of CO₂: Probing the Chemical State of the Ni(111) Surface during the Methanation Reaction with Ambient-Pressure X-Ray Photoelectron Spectroscopy. *J. Am. Chem. Soc.* **2016**,

- 138 (40), 13246–13252. (g) Peebles, D. E.; Goodman, D. W.; White, J. M. Methanation of carbon dioxide on nickel(100) and the effects of surface modifiers. *J. Phys. Chem.* **1983**, *87* (22), 4378–4387. (h) Roiaz, M.; Monachino, E.; Dri, C.; Greiner, M.; Knop-Gericke, A.; Schlögl, R.; Comelli, G.; Vesselli, E. Reverse Water–Gas Shift or Sabatier Methanation on Ni(110)? Stable Surface Species at Near-Ambient Pressure. *J. Am. Chem. Soc.* **2016**, *138* (12), 4146–4154. (i) Kim, H. Y.; Lee, H. M.; Park, J.-N. Bifunctional Mechanism of CO₂ Methanation on Pd–MgO/SiO₂ Catalyst: Independent Roles of MgO and Pd on CO₂ Methanation. *J. Phys. Chem. C* **2010**, *114* (15), 7128–7131. (j) Ren, J.; Guo, H.; Yang, J.; Qin, Z.; Lin, J.; Li, Z. Insights into the mechanisms of CO₂ methanation on Ni(111) surfaces by density functional theory. *Appl. Surf. Sci.* **2015**, *351*, 504–516.
- (8) (a) Kuzmin, A.; Mironova, N. Composition dependence of the lattice parameter in NiMg_{1–x}O solid solutions. *J. Phys.: Condens. Matter* **1998**, *10* (36), 7937–7944. (b) Kuzmin, A.; Mironova, N.; Purans, J.; Rodionov, A. X-ray absorption spectroscopy study of NiMg_{1–x}O solid solutions on the Ni K edge. *J. Phys.: Condens. Matter* **1995**, *7* (48), 9357.
- (9) Li, Y.; Lu, G.; Ma, J. Highly active and stable nano NiO–MgO catalyst encapsulated by silica with a core–shell structure for CO₂ methanation. *RSC Adv.* **2014**, *4* (34), 17420–17428.
- (10) (a) Yan, Y.; Dai, Y.; He, H.; Yu, Y.; Yang, Y. A novel W-doped Ni–Mg mixed oxide catalyst for CO₂ methanation. *Appl. Catal., B* **2016**, *196*, 108–116. (b) Nakayama, T.; Ichikuni, N.; Sato, S.; Nozaki, F. Ni/MgO catalyst prepared using citric acid for hydrogenation of carbon dioxide. *Appl. Catal., A* **1997**, *158* (1–2), 185–199. (c) Tomishige, K.; Himeno, Y.; Matsuo, Y.; Yoshinaga, Y.; Fujimoto, K. Catalytic Performance and Carbon Deposition Behavior of a NiO–MgO Solid Solution in Methane Reforming with Carbon Dioxide under Pressurized Conditions. *Ind. Eng. Chem. Res.* **2000**, *39* (6), 1891–1897.
- (11) Serra, M.; Salagre, P.; Cesteros, Y.; Medina, F.; Sueiras, J. E. Design of NiO–MgO materials with different properties. *Phys. Chem. Chem. Phys.* **2004**, *6* (4), 858–864.
- (12) (a) Tomishige, K.; Chen, Y.-g.; Fujimoto, K. Studies on Carbon Deposition in CO₂ Reforming of CH₄ over Nickel–Magnesia Solid Solution Catalysts. *J. Catal.* **1999**, *181* (1), 91–103. (b) Tomishige, K.; Yamazaki, O.; Chen, Y.; Yokoyama, K.; Li, X.; Fujimoto, K. Development of ultra-stable Ni catalysts for CO₂ reforming of methane. *Catal. Today* **1998**, *45* (1–4), 35–39. (c) Guo, M.; Lu, G. The effect of impregnation strategy on structural characters and CO₂ methanation properties over MgO modified Ni/SiO₂ catalysts. *Catal. Commun.* **2014**, *54*, 55–60.
- (13) (a) Takezawa, N.; Terunuma, H.; Shimokawabe, M.; Kobayashib, H. Methanation of carbon dioxide: preparation of Ni/MgO catalysts and their performance. *Appl. Catal.* **1986**, *23* (2), 291–298. (b) Arena, F.; Licciardello, A.; Parmaliana, A. The role of Ni²⁺ diffusion on the reducibility of NiO/MgO system: A combined TRP-XPS study. *Catal. Lett.* **1990**, *6* (1), 139–149.
- (14) Behrens, M. Coprecipitation: An excellent tool for the synthesis of supported metal catalysts – From the understanding of the well known recipes to new materials. *Catal. Today*.
- (15) Millet, M.-M.; Algara-Siller, G.; Wrabetz, S.; Mazheika, A.; Girgsdies, F.; Teschner, D.; Seitz, F.; Tarasov, A.; Levchenko, S. V.; Schloegl, R.; Frei, E. Ni single atom catalysts for CO₂ activation. *J. Am. Chem. Soc.* **2019**, *141* (6), 2451–2461.
- (16) Brunauer, S.; Emmett, P. H.; Teller, E. Adsorption of Gases in Multimolecular Layers. *J. Am. Chem. Soc.* **1938**, *60*, 309–319.
- (17) Millet, M.-M.; Frei, E.; Algara-Siller, G.; Schlögl, R.; Tarasov, A. Surface titration of supported Ni catalysts by O₂-pulse thermal analysis. *Appl. Catal., A* **2018**, *566*, 155–163.
- (18) (a) Geyer, R.; Hunold, J.; Keck, M.; Kraak, P.; Pachulski, A.; Schödel, R. Methods for Determining the Metal Crystallite Size of Ni Supported Catalysts. *Chem. Ing. Tech.* **2012**, *84* (1–2), 160–164. (b) Hoang-Van, C.; Kachaya, Y.; Teichner, S. J.; Arnaud, Y.; Dalmon, J. A. Characterization of nickel catalysts by chemisorption techniques, x-ray diffraction and magnetic measurements. *Appl. Catal.* **1989**, *46* (2), 281–296. (c) Webb, P. A. Introduction to Chemical Adsorption Analytical Techniques | Adsorption | Catalysis. *Scribd*. (d) Nakai, K. Pulse chemisorption measurement < Metal dispersion measurement >. *BEL-CAT Application note* 2003, CAT-APP-002.
- (19) Ball, M. C. The Dehydration of Brucite. *Mineral. Mag. J. Mineral. Soc.* **1961**, *32* (253), 754–766.
- (20) Bartley, J. K.; Xu, C.; Lloyd, R.; Enache, D. I.; Knight, D. W.; Hutchings, G. J. Simple method to synthesize high surface area magnesium oxide and its use as a heterogeneous base catalyst. *Appl. Catal., B* **2012**, *128*, 31–38.
- (21) (a) Carrott, M. R.; Carrott, P.; Carvalho, M. B. d.; Sing, K. S. W. Infrared and quantitative adsorption study of coordinatively unsaturated cations on magnesium hydroxide. *J. Chem. Soc., Faraday Trans.* **1993**, *89* (3), 579–583. (b) Carrott, M. R.; Carrott, P.; Carvalho, M. B. d.; Sing, K. S. W. Ex-hydroxide magnesium oxide as a model adsorbent for investigation of micropore filling mechanisms. *J. Chem. Soc., Faraday Trans.* **1991**, *87* (1), 185–191. (c) Carrott, M. M. L. R.; Carrott, P. J. M. Adsorption of Water Vapour by Microporous Magnesium Oxide. In *Stud. Surf. Sci. Catal.* Rouquerol, J., Rodríguez-Reinoso, F., Sing, K. S. W., Unger, K. K., Eds.; Elsevier: Amsterdam, 1994; Vol. 87, pp 497–506. (d) Ribeiro Carrott, M. M. L.; Carrott, P. J. M.; Brotas de Carvalho, M. M.; Sing, K. S. W. Microstructure of Ex-Hydroxide Magnesium Oxide & Products of Rehydration. In *Stud. Surf. Sci. Catal.* Rodríguez-Reinoso, F., Rouquerol, J., Sing, K. S. W., Unger, K. K., Eds.; Elsevier: Amsterdam, 1991; Vol. 62, pp 635–643. (e) Brett, N. H.; MacKenzie, K. J. D.; Sharp, J. H. The thermal decomposition of hydrous layer silicates and their related hydroxides. *Q. Rev., Chem. Soc.* **1970**, *24* (2), 185–207.
- (22) (a) Lra, R. R.; Clunie, J. S.; Goodman, J. F. Topotactic Dehydration of Brucite. *Nature* **1966**, *209*, 1083. (b) Green, J. Calcination of precipitated Mg(OH)₂ to active MgO in the production of refractory and chemical grade MgO. *J. Mater. Sci.* **1983**, *18* (3), 637–651. (c) KIM, M. G.; DAHMEN, U.; SEARCY, A. W. Structural Transformations in the Decomposition of Mg(OH)₂ and MgCO₃. *J. Am. Ceram. Soc.* **1987**, *70* (3), 146–154.
- (23) (a) Moodie, A. F.; Warble, C. E. MgO morphology and the thermal transformation of Mg(OH)₂. *J. Cryst. Growth* **1986**, *74* (1), 89–100. (b) Sutradhar, N.; Sinhamahapatra, A.; Pahari, S. K.; Pal, P.; Bajaj, H. C.; Mukhopadhyay, I.; Panda, A. B. Controlled Synthesis of Different Morphologies of MgO and Their Use as Solid Base Catalysts. *J. Phys. Chem. C* **2011**, *115* (25), 12308–12316. (c) Naono, H. Micropore formation due to thermal decomposition of magnesium hydroxide. *Colloids Surf.* **1989**, *37*, 55–70.
- (24) (a) Xiao, H.; Liu, Z.; Zhou, X.; Zhu, K. A unique method to fabricate Ni_xMg_{1–x}O (111) nano-platelet solid solution catalyst for CH₄–CO₂ dry reforming. *Catal. Commun.* **2013**, *34*, 11–15. (b) Fan, X.; Liu, Z.; Zhu, Y.-A.; Tong, G.; Zhang, J.; Engelbrekt, C.; Ulstrup, J.; Zhu, K.; Zhou, X. Tuning the composition of metastable CoxNiyMg100–x–y(OH)(OCH₃) nanoplates for optimizing robust methane dry reforming catalyst. *J. Catal.* **2015**, *330*, 106–119. (c) Zhu, K.; Hu, J.; Kübel, C.; Richards, R. Efficient Preparation and Catalytic Activity of MgO(111) Nanosheets. *Angew. Chem., Int. Ed.* **2006**, *45* (43), 7277–7281.
- (25) Mguni, L. L.; Mukenga, M.; Jalama, K.; Meijboom, R. Effect of calcination temperature and MgO crystallite size on MgO/TiO₂ catalyst system for soybean oil transesterification. *Catal. Commun.* **2013**, *34*, 52–57.
- (26) Zhang, X.; Zheng, Y.; Feng, X.; Han, X.; Bai, Z.; Zhang, Z. Calcination temperature-dependent surface structure and physico-chemical properties of magnesium oxide. *RSC Adv.* **2015**, *5* (105), 86102–86112.
- (27) (a) Arena, F.; Frusteri, F.; Parmaliana, A.; Giordano, N. On the reduction of NiO forms in magnesia supported catalysts. *React. Kinet. Catal. Lett.* **1990**, *42* (1), 121–126. (b) Jafarbegloo, M.; Tarlani, A.; Mesbah, A. W.; Muzart, J.; Sahebdehfar, S. NiO–MgO Solid Solution Prepared by Sol–Gel Method as Precursor for Ni/MgO Methane Dry Reforming Catalyst: Effect of Calcination Temperature on Catalytic Performance. *Catal. Lett.* **2016**, *146* (1), 238–248. (c) Parmaliana, A.; Arena, F.; Frusteri, F.; Giordano, N. Temperature-programmed reduction study of NiO–MgO interactions in magnesia-supported Ni

catalysts and NiO–MgO physical mixture. *J. Chem. Soc., Faraday Trans.* **1990**, 86 (14), 2663–2669.

(28) (a) Arena, F.; Frusteri, F.; Parmaliana, A.; Plyasova, L.; Shmakov, A. N. Effect of calcination on the structure of Ni/MgO catalyst: an X-ray diffraction study. *J. Chem. Soc., Faraday Trans.* **1996**, 92 (3), 469–471.

(b) Bond, G. C.; Sarsam, S. P. Reduction of nickel/magnesia catalysts. *Appl. Catal.* **1988**, 38 (2), 365–377.

(29) Lascelles, K.; Morgan, L. G.; Nicholls, D.; Beyersmann, D. Nickel Compounds. In *Ullmann's Encyclopedia of Industrial Chemistry*; Wiley-VCH Verlag GmbH & Co. KGaA: Berlin, 2000.

(30) Mazheika, A.; Levchenko, S. V. Ni Substitutional Defects in Bulk and at the (001) Surface of MgO from First-Principles Calculations. *J. Phys. Chem. C* **2016**, 120 (47), 26934–26944.

(31) Maçaira, J.; Mesquita, I.; Andrade, L.; Mendes, A. Role of temperature in the recombination reaction on dye-sensitized solar cells. *Phys. Chem. Chem. Phys.* **2015**, 17 (35), 22699–22710.

(32) (a) Vogt, C.; Groeneveld, E.; Kamsma, G.; Nachtegaal, M.; Lu, L.; Kiely, C. J.; Berben, P. H.; Meirer, F.; Weckhuysen, B. M. Unravelling structure sensitivity in CO₂ hydrogenation over nickel. *Nature Catalysis* **2018**, 1 (2), 127–134. (b) Miyao, T.; Shen, W.; Chen, A.; Higashiyama, K.; Watanabe, M. Mechanistic study of the effect of chlorine on selective CO methanation over Ni alumina-based catalysts. *Appl. Catal., A* **2014**, 486, 187–192. (c) da Silva, D. C. D.; Letichevsky, S.; Borges, L. E. P.; Appel, L. G. The Ni/ZrO₂ catalyst and the methanation of CO and CO₂. *Int. J. Hydrogen Energy* **2012**, 37 (11), 8923–8928.